ELSEVIER

Contents lists available at ScienceDirect

Sustainable Materials and Technologies

journal homepage: www.elsevier.com/locate/susmat





Printable ionic liquid modified cellulose acetate for sustainable chromic and resistive temperature sensing

B.D.D. Cruz ^{a,b,c}, A.S. Castro ^a, L.C. Fernandes ^b, N. Pereira ^b, C. Mendes-Felipe ^d, M. Tariq ^e, J.M.S.S. Esperança ^e, P.M. Martins ^{c,f}, S. Lanceros-Méndez ^{b,d,g,**}, D.M. Correia ^{a,*}

- ^a Centre of Chemistry, University of Minho, 4710-057 Braga, Portugal
- b Physics Centre of Minho and Porto Universities (CF-UM-UP) and Laboratory of Physics for Materials and Emergent Technologies (LapMET), University of Minho, 4710-057 Braga, Portugal
- ^c Centre of Molecular and Environmental Biology, University of Minho, 4710-057 Braga, Portugal
- d BCMaterials, Basque Center for Materials, Applications and Nanostructures, UPV/EHU Science Park, 48940 Leioa, Spain
- ^e LAQV, REQUIMTE, Departmento de Química, Faculdade de Ciências e Tecnologia, Universidade Nova de Lisboa, 2829-516 Caparica, Portugal
- f IB-S Institute for Research and Innovation on Bio-Sustainability, University of Minho, 4710-057 Braga, Portugal
- g Ikerbasque, Basque Foundation for Science, 48009 Bilbao, Spain

ARTICLE INFO

Keywords: Cellulose acetate Composites Ionic liquids Printing systems Thermochromism

ABSTRACT

Sustainable technologies and the circular economy paradigms require a reduction of waste, and therefore, research is focusing on the development of sustainable materials and devices capable of being reused, refurbished or recycled.

In the present work, printable ionic liquid (IL)-based polymer composites with thermochromic properties have been developed through a more sustainable approach to mitigate the negative impact of advanced functional materials and processes. For this purpose, composite films based on a natural polymer, cellulose acetate (CA), and different contents of the thermochromic IL, bis(1-butyl-3-methylimidazolium) tetrachloronickelate ([Bmim]_2[NiCl_4]), have been processed by a solvent casting method for the development of sustainable temperature sensors. The composites are transparent at room temperature, but when exposed to a temperature of 50 °C, the colour changes to blue. Incorporating the thermochromic IL led to the appearance of pores in the material's structure, which increased with increasing IL concentration. Additionally, the Young Modulus decreases with increasing IL concentration, reaching a value of 840 \pm 158 MPa) for the sample with 40 % wt. Contrarily, the electrical conductivity strongly increases with the highest DC electrical conductivity, with a maximum conductivity of 1.1 \times 10–5 \pm 1.5 \times 10–6 S.cm-1 obtained for the sample with 40 % wt. of [Bmim]_2[NiCl_4].

As a proof of concept, the potential applicability of the developed natural-based nanoparticle-free materials was demonstrated with a $CA/40[Bmim]_2[NiCl_4]$ sample by the development of printable thermochromic temperature sensors for thermotherapy applications in the temperature range from 33 °C to 50 °C.

1. Introduction

Nowadays, the demand for multifunctional materials, required by the interactivity and interconnectivity enabled by the Internet of Things (IoT) concept, has been increasing in different areas, namely energy [1], environment [2], biomedical [3], sensors [4] and actuators [5]. In particular, smart materials are particularly interesting in the area of

sensing, based on their ability to exhibit specific functional responses (e. g., colour change or development of electrical potential) triggered by changes in their surrounding (e.g. temperature or pressure variations) [6,7]. Among the different materials used to develop multifunctional materials, both synthetic and natural polymers have been commonly employed due to their easy processing, chemical stability, tailorable properties, and low cost [3,8].

E-mail address: dcorreia@quimica.uminho.pt (D.M. Correia).

^{*} Corresponding author at: Centre of Chemistry, University of Minho, Braga, 4710-057, Portugal.

^{**} Corresponding author at: Physics Centre of Minho and Porto Universities (CF-UM-UP) and Laboratory of Physics for Materials and Emergent Technologies (LapMET), University of Minho, 4710-057 Braga, Portugal.

Within the circular economy paradigm, materials with multifunctional properties should be developed that allow their implementation in more than one application after being processed, in another application after having been used, or recycled [9]. In fact, following these principles, biodegradable polymers, such as cellulose acetate (CA), a cellulose derivative, gained a significant importance [10] by promoting a reduction of the impact on the environment. Natural-based polymers combined with green solvents and being nanoparticle-free allow them to develop more sustainable multifunctional materials [11]. CA is an abundant biodegradable polymer obtained through the acetylation of cellulose, one of the essential cellulose derivatives, due to its intrinsic properties and wide application areas [12]. CA presents low toxicity, high chemical and mechanical stability, and solubility in diverse green solvents [13,14]. Cellulose and its derivatives offer design versatility due to the presence of hydroxyl groups that can be easily modified with other functional groups by hydrolysis, crosslinking reactions, and esterification, among others [15,16]. CA has been thus widely employed in the development of materials in areas such as biomedical [17], food packaging [18], environmental [19], and energy storage [20], among others.

The multifunctionality of many polymer-based materials results from the combination of a polymer matrix with distinct functional fillers, e.g., conductive powders, magnetic nanoparticles or dielectric particles [3]. Despite nanoparticles possessing an enormous potential to be applied in different fields, several issues related to their toxicity, genotoxicity, and ecotoxicity have been massively reported in the literature over the last decades, indicating the undesirable impact on humans and the environment [21-23].

In this context, ionic liquids (ILs) arise as an exciting approach due to their attractive properties, which include high thermal stability, low toxicity, high viscosity, and negligible vapour pressure at room temperature [24]. Also, IL allow multiple combinations of different cations and anions with distinct functionalities to yield different physical-chemical properties [25,26] (e.g., solubility, viscosity, density) and active-response (e.g. magnetic [27], luminescent [28], piezoionic [29], thermochromic [30]).

ILs with thermochromic properties able to change their colour with temperature have been explored through their incorporation into different polymer matrixes, such as photocurable polymers, aiming their potential to be applied in smart packaging, actuators, and sensors [29–32]. Despite these efforts, there is a lack of studies exploring their scalability to printing technologies.

In recent years, new approaches aiming at developing materials with better performance, miniaturization and more environmentally friendly devices have led to the search for novel materials and novel processing techniques [5]. In this context, additive manufacturing (AM) is mainly explored, as it allows the manufacture of devices and components sustainably by strongly reducing materials waste [1]. AM enables the conversion of digital data into physical objects, manufactured layer by layer, opening new opportunities for the industry, namely more efficient manufacturing of products from pre-defined files, with greater design freedom and great environmental benefits [33,34]. Direct ink writing (DIW) is a particular class of additive manufacturing technologies that allows the development of precise, cost-effective complex structures. In particular, the printing of IL-based solutions by DIW has emerged as a relevant technique for developing functional materials for several fields of application, including energy, sensors and actuators [35]. This method has been effectively used in developing ionogels [36] for wearable soft sensors such as electronic skins [37]. Besides ILs being characterized by their high viscosity, for printing technologies, in which the viscosity is a critical parameter, ionic liquid, polymer and solvent ratios must be taken into consideration to achieve the required viscosity for stable printing while maintaining the necessary amount of functional material for proper functional response.

In this work, considering the demand to develop more sustainable alternatives to mitigate the negative impact of processed materials, thermochromic materials based on CA and bis(1-butyl-3-methylimidazolium) tetrachloronickelate ([Bmim] $_2$ [NiCl] $_4$) are proposed for temperature sensing applications based on colour variation. The IL was selected based on its thermochromic characteristics, including colour and transition temperature [29,30]. The effect of IL content on the morphological, physicochemical, mechanical, and electrical properties of the processed materials was evaluated, and its potential applicability in sensor applications has been demonstrated. This study contributes to developing a new generation of natural polymer-based sensors that are processable by additive manufacturing for a wide range of applications.

2. Experimental section

2.1. Materials

The cellulose acetate (acetylcellulose, CA), with an acetyl content of 39.7~% wt. (Sigma Aldrich, average Mn ~ 50.000 by GPC) was purchased from Sigma Aldrich. The IL bis(1-butyl-3-methylimidazolium) tetrachloronickelate, [Bmim]₂[NiCl₄], (99 % purity) was synthesized as reported in [38,39]. The solvent acetone (99.7 %) was purchased from Merck.

2.2. Films production

CA and CA/[Bmim] $_2$ [NiCl $_4$] composites were prepared by a solvent casting method [30]. For neat CA film, 1 g of CA was added to 10 mL of acetone under magnetic stirring at 30 °C. To prepare CA-composites, 10, 20 and 40 % wt. of [Bmim] $_2$ [NiCl $_4$] were dispersed in acetone, and then, the CA was added. After the complete polymer dissolution, the solution was poured into a glass and spread, followed by overnight solvent evaporation at room temperature. After this procedure, films with a thickness between 26 and 49 μ m were obtained. The thickness was obtained by measuring the samples in triplicate using a micrometre (Fisher, DKD-K-33101).

2.3. Functional prototype development

Screen printing was used on a PET substrate (Dupont Teijin Melinex 506), a heater with a length of 100 mm, and an interdigit with a channel length of 145 mm and a width of 500 μm . Silver ink (Metalon® HPS-021LV from Novacentrix) and a screen mesh with a density of 100 threads per centimetre were used for this process. The printed patterns were subsequently cured in an electric convection oven (P-Selecta) for one hour at 80 $^{\circ} C$.

The thermochromic printable materials based on CA/[Bmim] $_2$ [NiCl $_4$] solutions (prepared as briefly described and schematised in steps 1 and 2 of Fig. 1), with different IL contents, were printed as a rectangle on the back side of the printed heater (other side of the PET substrate) on top of the interdigit using a 3D deposition printer that was modified from the Tenlog TL-D3 model (step 3 and 4). The illustration of the processing of the sample is demonstrated in Fig. 1.

Samples having an approximate thickness of 190 \pm 10 μm were acquired after air drying at ambient temperature. The printed parameters, obtained after an optimisation procedure, are presented in Table 1.

2.4. Physical-chemical characterization

The morphology of the CA based materials was evaluated using a scanning electron microscope (SEM) Carl Zeiss EVO-40 equipment, with an accelerating voltage of 20 kV. Previously, the samples were coated with a thin layer of gold using sputter coating (Polaron SC502). Energy-dispersive X-ray (EDX) analysis was carried out in a SEM Carl Zeiss EVO-40 with EDX de Oxford Instruments.

The materials' wettability was estimated by measuring the contact angle (3 replicates) of a drop of distilled water (3 μ L) at room

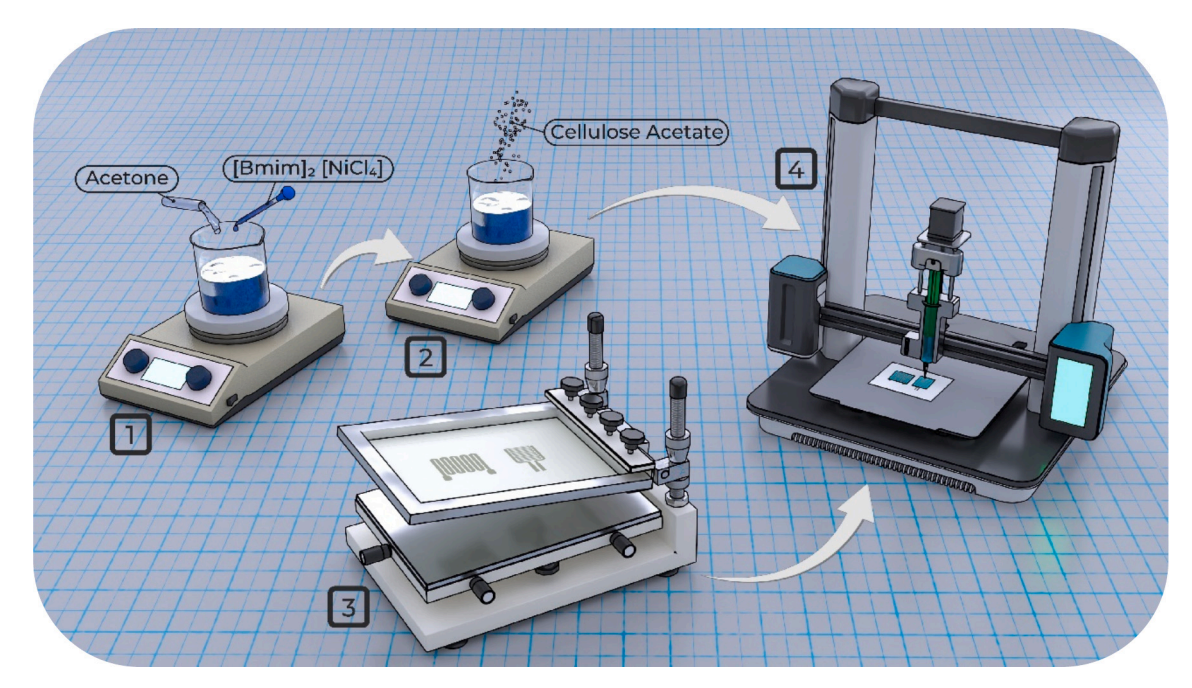


Fig. 1. Schematic representation of procedure to develop CA and CA/[Bmim]₂[NiCl₄] films by DIW.

Table 1
Printing parameter for the CA/IL composites on the modified Tenlog TL-D3 printer.

Slicer software	Ultimaker Cura 5.5
Needle Tip Printing speed Flow Infill Density Infill Pattern Infill layer Thickness	0.9 mm 30 mm/s 30 % 80 % Concentric 0.2 mm
Top/Bottom Thickness	0 mm
Wall Thickness	0 mm
Temperature	Room
	temperature
	Needle Tip Printing speed Flow Infill Density Infill Pattern Infill layer Thickness Top/Bottom Thickness Wall Thickness

temperature using a DataPhysics OCA 20 contact angle system.

The attenuated total reflection Fourier transform infrared (ATR-FTIR) spectra were evaluated using an ALPHA II spectrometer in the 4000 and 400 cm^{-1} range, using 64 scans and a resolution of 4 cm^{-1} . XRD patterns were recorded with a Philips 'X'Pert MPD Powder detector in the 20 range of 10° to 80° at room temperature. Monochromated Cu K α radiation (λ =1.541 Å) was used with a resolution of 0.02° . The samples were not subjected to any thermal pre-treatment before analysis. Differential scanning calorimetry (DSC) thermograms were evaluated in a Mettler Toledo 822e calorimeter, between 25 and 400 °C, at a heating rate of 10 °C/min in a high nitrogen atmosphere at a constant flow of 20 mL/min. The UV–Vis spectra of CA-based films and composites were recorded with a UV-2501PC Spectrophotometer (Shimadzu) at room temperature at 200–900 nm.

The mechanical properties of the films were assessed in the tensile mode, in triplicate at room temperature, using rectangular shape samples (thickness between 26 and 49 μ m; 30 mm \times 10 mm) in a Linkam Scientific Instruments TST 360 testing machine (Temperature-Controlled), comprising a Tensile Stress Testing Stage, at a speed of 15 mm/s

The volumetric electrical conductivity of the samples was evaluated using an automated Keithley 487 picoammeter/voltage source,

measuring the characteristic current-voltage curves (I–V) at room temperature by applying voltages ranging from -10 to +10 V. Previously, gold electrodes with 5 mm circular diameter were coated on both sides by magnetron sputtering (Scancoat Six SEM Sputter Coater). The electrical conductivity values were achieved from the I—V slope using Eq. (1):

$$\sigma = \frac{1}{\left(\frac{R \times A}{L}\right)} \tag{1}$$

The heater conductivity was evaluated using a Keithley 2400 Source meter connected directly to the printed heater, applying a current between -1 to 1 mA and reading the voltage.

2.5. Functional prototype development and testing

The heater joule effect performance was evaluated using a Keithley 2400 Sourcemeter, applying a current from 0 to 125 mA and monitoring the voltage drop (due to resistance variation with the temperature) for calculating the amount of energy produced by the joule effect (Eq. (2))

$$Q = I^2 \times R \times t \tag{2}$$

where Q indicates de joule energy, I is the applied current, R is the heater's resistance, and t is the time in seconds.

The electrical resistance variation with the temperature of the CA/IL composites was evaluated using an Agilent 34401 A multimeter. The temperature was controlled with a Linkam THMSE 600 at a rate of $10~^{\circ}\text{C/min}$.

The colour intensity was evaluated using a Logitech C615 HD Webcam, and colour variations were analyzed by the ImageJ colour histogram function on the RGB colour space and converted in Matlab to the CIE 1931 Chromaticity Diagram.

3. Results and discussion

3.1. Samples morphology

The morphology of the prepared films was evaluated by SEM technique, as presented in the cross-sectional images in Fig. 1 for CA and CA/[Bmim] $_2$ [NiCl $_4$] composites with different concentrations of

[Bmim]₂[NiCl₄] (10, 20 and 40 % wt.).

The pure CA film (Fig. 2a) presents a smooth, non-porous and dense morphology related to the low boiling point of acetone [37], leading to the polymer chain occupying the free space left by the acetone, not inducing the phase separation. With the incorporation of [Bmim]₂[-NiCl₄] into the polymer matrix, the films morphology suffers significant alterations, with IL leading to the formation of pores, regardless of their quantity, as shown in Fig. 2b-d. The porous structure results from the interactions between the IL-solvent, leading to a liquid-liquid polymer phase separation. During this phase separation process, the strong ILsolvent interaction leads to an excess of IL in the solvent-rich regions that remain in the pores after solvent evaporation and polymer crystallisation [40]. Similar results were observed by incorporating the [Bmim]₂[NiCl₄], IL, into a different matrix such as poly (vinylidene fluoride), PVDF, whose porous structure is due to interactions of ILsolvent, leading to phase separation [41]. This IL was also incorporated into a photo resin matrix (polyurethane acrylated), and it was observed that the [Bmim]₂[NiCl₄] also causes the formation of a porous structure that increases with the increase in the IL content [29].

SEM-EDX mapping, displayed in Fig. 3, accessed the dispersion and distribution of the ILs in the different CA composite films.

As shown in Fig. 3, all the samples present the characteristic elements of the IL $[Bmim]_2[NiCl_4]$, nickel (Ni) and chlorine (Cl). Both elements are well dispersed and evenly distributed in the matrix, and as expected, as the percentage of IL within the films increased, there was also an increase in the amount of Ni and Cl in the polymer matrix. This increase is also correlated with the SEM images of Fig. 2, in which an increase in the porous structure is observed with the IL content increase.

3.2. Surface wettability

Modifications in the surface roughness and surface chemistry contribute to differences in the surface wettability of the composites [42]. This wettability was evaluated using the sessile-drop technique, which consists of measuring the contact angle of the water droplet with the film's surface [43]. A contact angle above 90° indicates a hydrophobic surface, while a contact angle below 90° indicates a hydrophilic surface [44,45]. The results of the CA and CA composites are presented

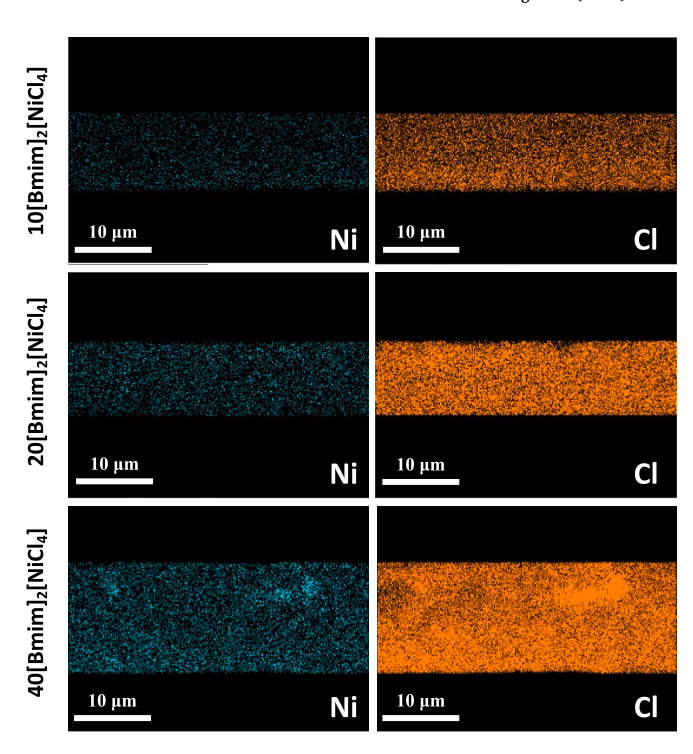


Fig. 3. EDX mapping images of Ni and Cl elements along the cross-section of $CA/[Bmim]_2[NiCl_4]$ (10, 20, 40 % wt.) films.

in Fig. 4a.

Fig. 4a shows that both CA and CA composites are characterized by a hydrophilic behaviour. Given the hygroscopic nature of IL [46], this can be proven by the absorption band located between 3400 and 3600 cm⁻¹ in the ATR-FTIR spectra. Nonetheless, and despite the increase in pores in the samples with an increase in the concentration of IL incorporated, which could lead to an increase in surface wettability [47], this does not occur. This can be explained by the repulsive interactions of the polar water molecules with the cation [Bmim]⁺ of the IL, promoting a slight

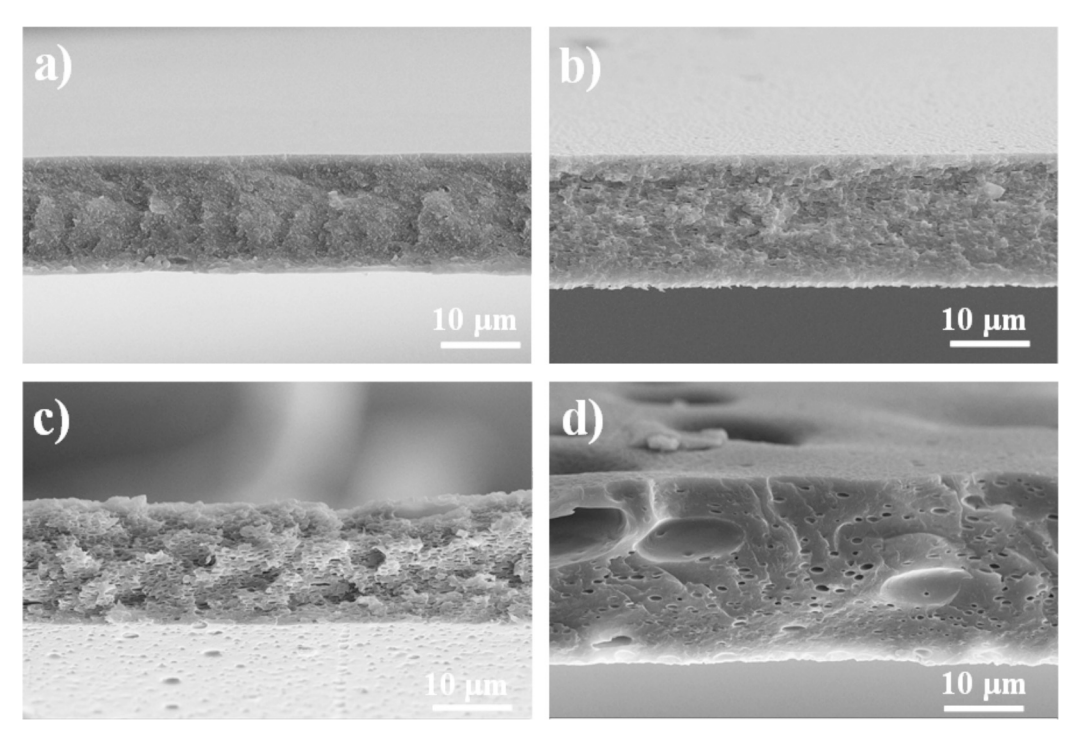


Fig. 2. Cross-section SEM images of CA (a) and CA/[Bmim]₂[NiCl₄] composites with 10 % wt. (b), 20 % wt. and (c) 40 % wt. (d) IL content.

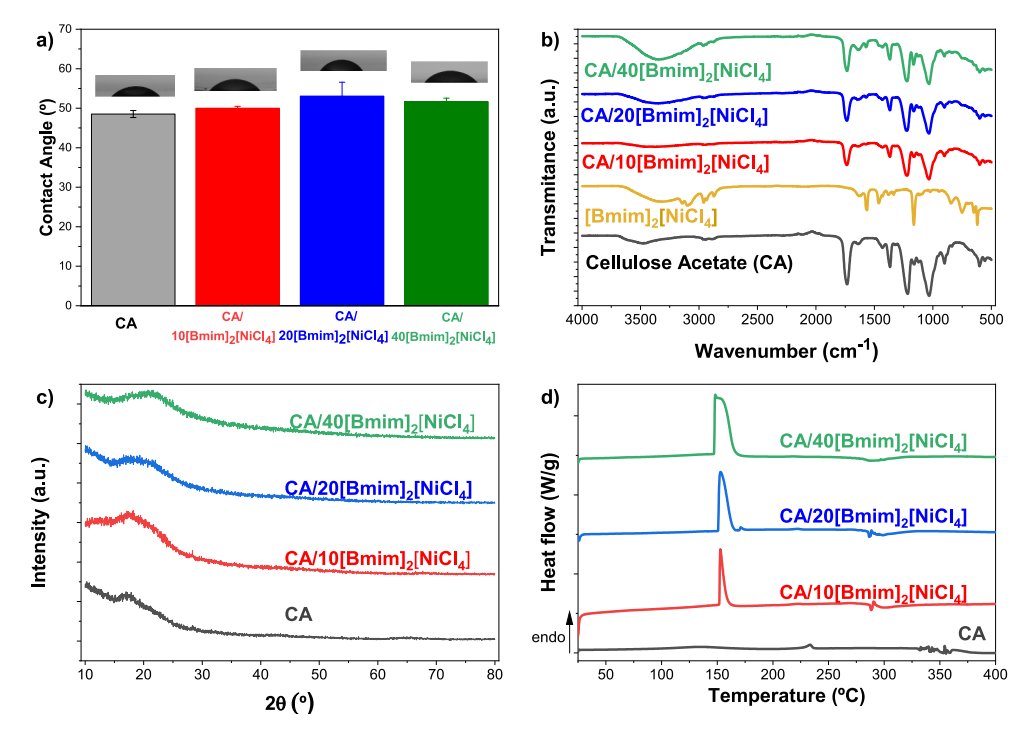


Fig. 4. a) Surface wettability, b) ATR-FTIR spectra, c) XRD patterns, and d) DSC curves of CA and CA/[Bmim]₂[NiCl₄] composite films.

increase in contact angle compared with the pure CA samples [48].

3.3. Physical-chemical characterization

ATR-FTIR measurements, shown in Fig. 4b, evaluated the influence of the $[Bmim]_2[NiCl_4]$ on the CA chemical characteristics.

The typical CA absorption bands are observed for all samples, the broad absorption band located between 3400 and 3500 cm⁻¹ being attributed to unacetylated cellulose's hydroxyl groups (-OH) stretching [49]. This band increases their intensity with increasing IL content, corresponding to the stretching and bending vibration modes of the $\mathrm{H}_2\mathrm{O}$ molecules, indicating the high sensitivity to the humidity of the IL [30]. Between 2900 and 2950 cm⁻¹, the absorption band characteristic of the C-H stretching of CH2 or CH3 is observed. The absorption band at 1734 cm⁻¹ is ascribed to the carbonyl group (C=O) stretching vibration of the -COCH₃ group and corresponding to the stretching of the acetyl group [49,50]. The peak at 1432 cm $^{-1}$ is associated with -CH₂- deformation vibration, and peaks at 1368 cm⁻¹ and 1216 cm⁻¹ correspond to CH₃ groups of the acetyl moiety [49,51]. The absorption band appearing at 1032 cm⁻¹ corresponds to the ether C-O-C bonds of the glycosidic bond [51]. The peaks at 953 cm⁻¹ and 900 cm⁻¹ are related to C—O and -C-OH stretching vibration, respectively [49].

The absorption bands at 2964, 2941, and 2878 cm $^{-1}$ correspond to the stretching vibrations of -C-H in both $-CH_2$ and $-CH_3$ groups from the IL, located near the nitrogen atoms within the imidazolium ring. Additionally, stretching vibrations of the $-CH_2$ groups stemming from the imidazolium ring are present at 3140 and 3098 cm $^{-1}$, while the skeletal vibrations are observed in the range of 1600 to 1340 cm $^{-1}$ [30]. This confirms the good incorporation of the IL into the CA films, even when contents up to 40 % wt. IL are used.

The XRD patterns of neat CA and CA composites are represented in Fig. 4c. Neat CA exhibits a weak peak at $2\theta=18-22^\circ$ since CA presents a degree of substitution of ~ 2.5 , in which most of the hydroxyl groups in cellulose are replaced by acetyl groups, leading to absent or minimal intermolecular hydrogen bonding, destroying the ordered crystalline structure [52]. Incorporating different contents of [Bmim]₂[NiCl₄] does not significantly alter the crystalline structure of the composite materials, as the peaks remain practically unchanged. This phenomenon has

already been observed in similar studies with cellulose and ILs [53].

The influence of the IL on the melting behaviour of CA and the corresponding composites was also evaluated by DSC (Fig. 4d). The melting temperature (T_m) of pristine CA films occurs at around 227 °C [54]. CA presents acetyl groups that influence the weakening of hydrogen bonds and improve the movement of the cellulose molecular chain, thus resulting in its melting [55]. With the incorporation of [Bmim] $_2$ [NiCl $_4$], an endothermic peak between 150 and 170 °C is observed, which increases with the IL content [56]. The appearance of this endothermic peak is related to the water desorption process, indicating, in this case, a reversible desorption of water in Ni(II) compounds in which H_2 O molecules are coordinated with metal ions [29,57]. As reported by related studies, the absorption and desorption process leads to changes in the Ni(II) coordination number from octahedral to tetrahedral structure [30]. From the DSC thermograms, it is not observed the glass transition of the CA that commonly appears at 200 °C.

3.4. Mechanical properties

The mechanical properties of $CA/[Bmim]_2[NiCl_4]$ films were evaluated by tensile stress versus strain curves to investigate the role of IL in composite mechanical response.

Fig. 5a shows the stress-strain curves, and Table 2 shows Young's modulus (E), maximum tensile stress (σ_v) and elongation at break (ϵ_b).

All materials show increased strain with the applied tensile strength increase, with the elongation at break dependent on the IL content. The pure CA film shows rigid behaviour, with poor extensibility, with an E, σ_y , and ϵ_b being 1909 ± 344 MPa, 75.77 MPa, and 11.07%, respectively, being the obtained values in agreement with the literature [58]. From Fig. 5a and Table 2, it is observed that upon the incorporation of IL, the elongation at break increases from 11.07 (pure CA) to 21.40 %, accomplished by a decrease in the maximum tensile stress (from 75.77 to 23.88 MPa), leading to a decrease of E with the increase of IL content, being this decrease more noticeable with the IL content increase up to 40 % wt. of [Bmim]_2[NiCl_4] (840 \pm 158 MPa).

The decrease in Young's modulus is indicative of the plasticising effect promoted by the [Bmim]₂[NiCl₄] [29]. However, when higher amounts of IL are added, the maximum elongation decreases from 24.5

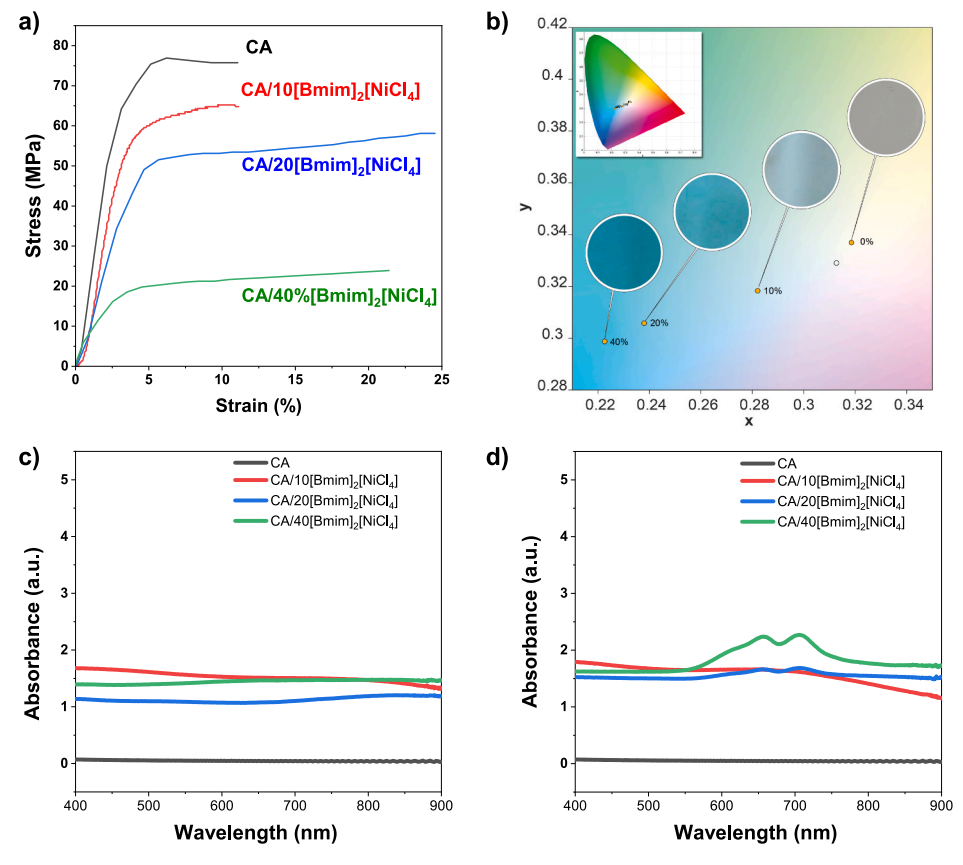


Fig. 5. a) Stress versus strain curves of CA and CA/[Bmim]₂[NiCl₄] composites, b) Colour intensity as a function of IL content. c and d) UV–Vis spectra of CA/[Bmim]₂[NiCl₄] composites with different IL contents at c) room temperature and d) 50 °C.

Table 2 Young modulus of CA and $CA/[Bmim]_2[NiCl_4]$ composites with different IL contents.

Membranes	E [MPa]	σ _y [MPa]	ε _b (%)
CA	1909 ± 344	75.77	11.07
CA/10[Bmim] ₂ [NiCl ₄]	1672 ± 185	64.78	11.13
CA/20[Bmim] ₂ [NiCl ₄]	1356 ± 139	58.13	24.53
$CA/40[Bmim]_2[NiCl_4]$	840 ± 158	23.88	21.40

% for the sample incorporating 20 % wt. of IL to 21.40 % for the CA/40 [Bmim]₂[NiCl₄] composite. Thus, the addition of IL induces variations in the morphologies of the polymer matrix, resulting in increasingly porous structures and, consequently, the materials have lower levels of elasticity [59]. All the films show elastic properties and do not become brittle when different amounts of IL are introduced despite their increasing porosity.

3.5. Thermochromism effect

The IL $[Bmim]_2[NiCl_4]$ is characterized by reversible thermochromic properties. As observed in Fig. 5b, regardless of the IL content, all the developed composites present a colour change from transparent to dark blue, with the colour intensity proportional to the IL content.

A UV–Vis analysis was performed to study the influence of temperature on the complex geometry of the IL anion, which is responsible for the thermochromic effect [29,30]. Fig. 5c and d show the UV–Vis spectra at room temperature and 50 °C of the CA and CA composite films. Heating at 50 °C was used considering the intended application in thermotherapy and based on previous studies in related materials [30]. Upon the processing of composites, and independently of IL content, the

films are colourless. Still, upon heating up to 50 $^{\circ}$ C, the composites change their colour, being this change a reversible and temperature-dependent process.

The observed thermochromism effect is explained by the desorption and absorption of water from the air. As observed from UV–Vis curves, no absorption band is observed at room temperature. However, independently of the IL content, when subjected to a temperature of 50 °C, two absorption peaks appeared at 656 and 707 nm. Being these peaks attributed to the $\left[\text{NiCl_4}\right]^{2-}$ complex in its tetrahedral conformation (blue region of UV–Vis spectrum). The appearance of the two absorption bands with increasing temperature indicates the colour change of the films from colourless to blue since no absorption peaks are seen in the UV–vis spectrum at room temperature [29,30]. The peaks have similar intensities. Increasing [Bmim]₂[NiCl₄] content increases the intensity of the absorption peaks.

Thus, the colour change of the composites is directly related to the modification of the IL coordination reaction, attributed to the absorption/desorption of water from the $[\mathrm{NiCl_4}]^{2-}$, associated with the variation in the coordination number of the Ni (II) from octahedral to tetrahedral, depending on the hydrated ($[\mathrm{Ni}\ (\mathrm{H_2O})_{6}]^{2+})$) or dehydrated ($[\mathrm{Ni}\ (\mathrm{H_2O})_{6}]^{2-})$) state [30]. This change in nickelate configuration by the absorption and desorption process can also be corroborated by the ATR-FTIR spectrum, in which the absorption band corresponding to O—H groups is present. It is also worth noting that the thermochromic effect is humidity-governed, as the humidity variation sets the colour change at each temperature, presenting a humidity system dependence. Further, it is also temperature-activated, the colour change also depends on the system temperature [29].

3.6. Electrical properties

The electrical properties of CA and CA/[Bmim]₂[NiCl₄] were evaluated by the current versus voltage (I-V) curves (Fig. 6).

As shown in Fig. 6a, the addition of IL into CA induces changes in the I-V curves from a linear to a non-linear regime. Similar results were observed for cellulose nanocrystal (CNC)/IL composites [5,60]. This non-linear regime is characterized by three main regions: one for lower voltages (i), one between $-2.0\ V$ and $2.0\ V$ (ii), and another for higher voltages (iii). These regions become more noticeable with increasing IL content. The variation in slopes observed upon the incorporation of IL can be attributed to the mobility of both the IL cation and anion within the CA matrix. The strong interactions between the IL and the CA matrix affect this mobility. Specifically, when the applied voltage is below $-2.0\ V$ or above $2.0\ V$, these strong interactions favour enhanced mobility, allowing the electrostatic interaction between the IL and the polymer to be surmounted.

The IL content and CA charge's effect on the electrical conductivity of the CA and CA composite samples was evaluated from the slope of I—V curves, Fig. 6b. It is observed that the DC electrical conductivity increases with the incorporation of IL in the CA matrix $(1.9\times10^{-13}\pm1.0\times10^{-15}~\rm S.cm^{-1}$ for pristine CA), increasing with increasing IL content. The increase in the electrical conductivity value occurs in all three regimes, being more notable for regimes (i) and (iii). The highest DC electrical conductivity values are observed for the sample with 40 % wt. of [Bmim]₂[NiCl₄], being: $1.1\times10^{-5}\pm1.5\times10^{-6}~\rm S.cm^{-1}$ (regime i), $3.0\times10^{-6}\pm1.9\times10^{-7}~\rm S.cm^{-1}$ (regime ii), and $8.7\times10^{-6}\pm2.2\times10^{-7}~\rm S.cm^{-1}$ (regime iii). This behaviour has also been observed for other naturally derived materials [61].

4. Proof of concept for thermotherapy on finger

Based on colour intensity and higher conductivity, the CA/ $[Bmim]_2[NiCl_4]$ composite film with 40 % wt. of IL was selected to obtain electrical resistance as a function of temperature (Fig. 7a-c) and evaluate the material's potential not just as a thermochromic sensor but also as a thermo-resistive material.

The Joule heater has a total resistance of 20 Ω and a slight increase in the resistance for the operational temperature range (30 to 50 °C) of approximately 0.026 Ω .°C⁻¹. The printed heater could generate a maximum temperature of around 50 °C for an input energy of 20 J.

The colour was assessed by analyzing the samples' colour histogram (Fig. 7d) at various temperatures. The colour histogram shows that when the temperature increases, there is a rise to the blue zone. This result suggests that with increasing temperature, the colour of the samples transitions towards a cooler and more vivid blue shade. Hence, temperature significantly influences the colour properties of the samples [30].

The CA/40[Bmim] $_2[NiCl_4]$ sample printed on top of the interdigit allowed the evaluation of the composite resistance as a function of the temperature variation, evaluated from 10 to 65 °C. As shown in Fig. 7e and f, the resistance of the composite drops as the temperature increases. This effect is commonly observed in related IL/polymer composites, in which the electrical conductivity increases with increasing temperature due to increased mobility of the ionic species [30]. The IL sample sensitivity is at approximately $-507~\Omega.^{\circ}\text{C-1}$ for an interdigit with a channel of 145 mm in length and 500 μm width. Also, by analyzing Fig. 7f, it is possible to note a higher error in the measurement for the low-temperature range. Thus, though further optimisation may be necessary to improve the stability and accuracy of the system, these results lay the foundation for a new generation of temperature sensors based on natural polymers and/or their derivatives.

The solution with the highest IL content was selected to be printed by DIW, as it displays a more intense blue colour upon heating (Fig. 8 and video S1). The developed heater with the thermochromic layer was attached to a finger joint. In clinical applications, the temperature required to increase extensibility is above 40 °C (40 to 45 °C) and maintained for at least 5 min [62]. The heater's power was controlled based on the previous experience to be below 50 °C, controlling the applied current and preventing the probability of skin burns [63]. The current was applied directly to the heater by a Keithley 2400 sourcemeter.

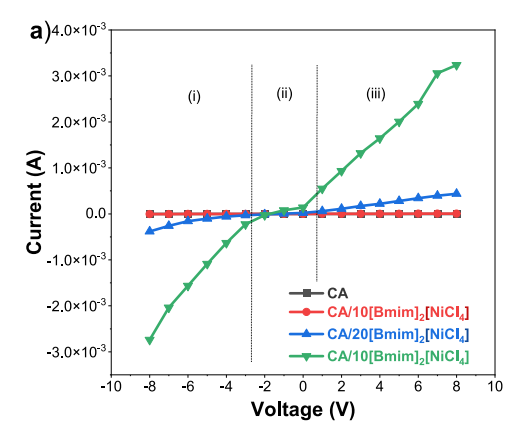
The thermochromic material starts to change colour around 35 $^{\circ}$ C with a lighter blue hue that shifts to a more saturated blue hue with increasing temperature and time. This colour change allows the patient to be visually aware of the temperature increase.

5. Conclusions

Smart and multifunctional natural-based materials combined with ionic liquids are suitable for sustainable digitalization. In this work, a temperature-sensing application has been successfully developed by combining screen printing and DIW techniques.

With the incorporation of [Bmim]_2[NiCl_4] in the cellulose acetate matrix, a porous structure is obtained without relevant physical-chemical changes in the polymer matrix or the IL. Furthermore, the incorporation of IL influences the mechanical and electrical properties. An increase in the electrical conductivity is observed with the incorporation of IL in the CA matrix from $1.95\times10^{-13}\pm1.07\times10^{-15}~Scm^{-1}$ for pristine CA to a maximum value of $1.14\times10^{-5}\pm1.54\times10^{-6}~S.~cm^{-1}$ for the sample with 40 % wt. [Bmim]_2[NiCl_4]. Further, the Young Modulus decreases with increasing IL content, from 1909.5 \pm 344.5 MPa for the pristine CA sample to 840.4 \pm 158.1 MPa for the sample with 40 % wt. [Bmim]_2[NiCl_4] content.

A thermochromic effect was observed for composites containing different IL contents. This process is directly related to the absorption/



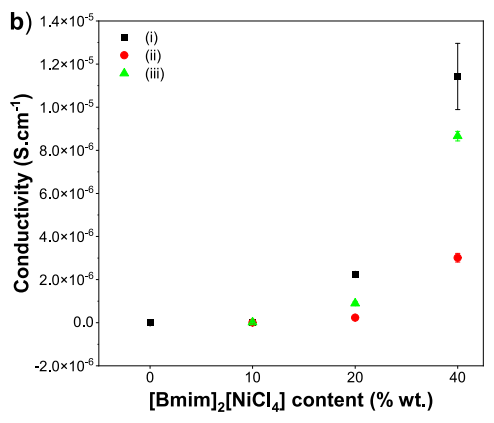


Fig. 6. a) Current vs voltage curves and b) electrical conductivity of the CA/[Bmim]₂[NiCl₄] composites as a function of [Bmim]₂[NiCl₄] content.

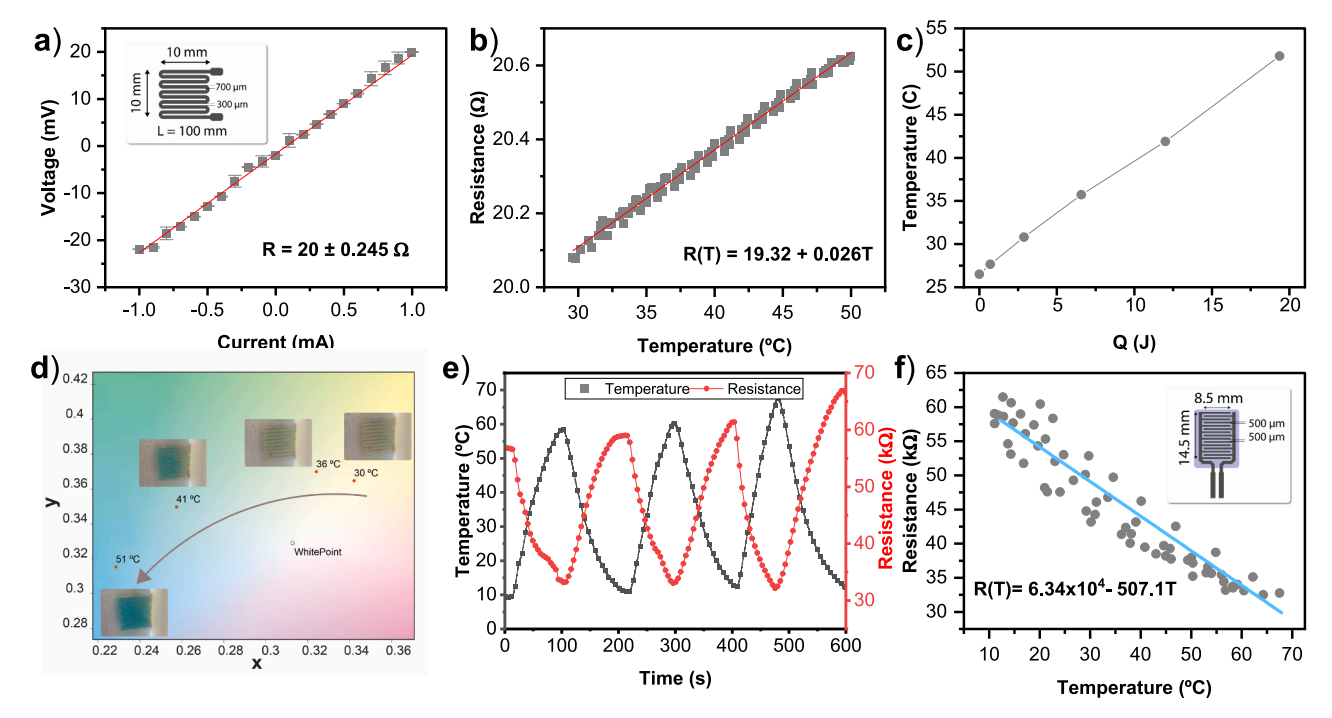


Fig. 7. a) Printed heater I-V curves, b) Heater resistance variation with temperature, c) produce temperature by the heater by joule effect, d) Colour Histogram variation with the applied temperature from the heater, e) Temperature cycles from 10 to 65 °C applied to the CA/40[Bmim]₂[NiCl₄]. f) Resistance variation of the CA/[Bmim]₂[NiCl₄] as a function of the applied temperature.

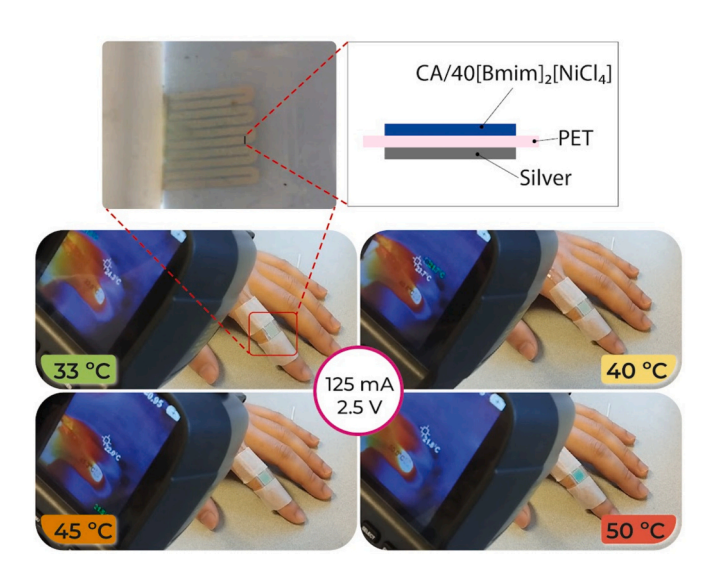


Fig. 8. Demonstration of the potential of CA/40[Bmim] $_2$ [NiCl $_4$] DIW printed sample for thermotherapy applications with a temperature variation from 33 $^{\circ}$ C to 50 $^{\circ}$ C within 84 s.

desorption of water from the $[NiCl_4]^{2-}$, which is associated with the variation in the coordination number of the Ni (II) from octahedral to tetrahedral depending on the hydrated ($[Ni\ (H_2O)_6]^{2+}$) or dehydrated ($[NiCl_4]^{2-}$) state.

The composite material exhibits a significant degree of colour change with the concentration of IL. This variation is more pronounced at greater concentrations of IL and is positively related to increased electrical conductivity.

The developed composite materials enable the advancement of thermochromic sensing with associated thermoresistive response, allowing applications as optical temperature sensors for thermotherapy in the temperature range from 33 $^{\circ}\text{C}$ to 50 $^{\circ}\text{C}$. Thus, this work

demonstrated the suitability of natural polymers, cellulose acetate, and hybrid materials for smart and multifunctional materials sensor applications by additive manufacturing technologies.

Supplementary data to this article can be found online at https://doi.org/10.1016/j.susmat.2024.e01101.

CRediT authorship contribution statement

B.D.D. Cruz: Data curation, Formal analysis, Investigation, Writing – original draft. A.S. Castro: Data curation, Formal analysis, Investigation, Writing - original draft. L.C. Fernandes: Data curation, Formal analysis, Investigation, Writing - original draft. N. Pereira: Data curation, Formal analysis, Investigation, Writing - original draft. C. Mendes-Felipe: Data curation, Formal analysis, Investigation, Writing – original draft. M. Tariq: Formal analysis, Investigation, Writing – original draft. J.M.S.S. Esperança: Formal analysis, Investigation, Writing – original draft. P.M. Martins: Formal analysis, Investigation, Writing - original draft. S. Lanceros-Méndez: Conceptualization, Methodology, Formal analysis, Funding acquisition, Investigation, Project administration, Resources, Supervision, Validation, Writing - original draft, Writing review & editing. D.M. Correia: Conceptualization, Methodology, Formal analysis, Funding acquisition, Investigation, Project administration, Resources, Supervision, Validation, Writing - original draft, Writing – review & editing.

Declaration of competing interest

The authors declare that they have no known competing financial interests or personal relationships that could have appeared to influence the work reported in this paper.

Data availability

Data will be made available on request.

Acknowledgements

Portuguese Foundation for Science and Technology (FCT): UID/FIS/ 04650/2020, UID/QUI/00686/2020, UIDB/04050/2020, 10.54499/LA/P/0008/2020, 10.54499/UIDP/50006/2020, 10.54499/UIDB/0006/2020, and 10.54499/2022.05932.PTDC. B.D.C., L,F., P. M. and D.M.C. also thank the FCT for financial support in the framework of the grant 2022.13287.BD, SFRH/BD/145345/2019 and the contracts 10.54499/2020.02802.CEECIND/CP1600/CT0017 and 10.54499/2020.02915.CEECIND/CP1600/CT0029, respectively.

This study forms part of the Advanced Materials program and was supported by MCIN with funding from European Union NextGenerationEU (PRTR-C17·I1) and by the Basque Government under the IKUR program and though the POSTDOC fellowship program (POS-E_2021_2_0001). Funding from the Basque Government Industry Department under the ELKARTEK program is also acknowledged. Technical and human support provided by SGIker (UPV/EHU, MICINN, GV/EJ, EGEF, and ESF) is gratefully acknowledged.

References

- [1] R.S. Pinto, J.P. Serra, J.C. Barbosa, R. Gonçalves, M.M. Silva, S. Lanceros-Méndez, et al., Direct-ink-writing of electroactive polymers for sensing and energy storage applications, Macromol. Mater. Eng. 306 (2021) 2100372.
- [2] J.P. Serra, A. Fidalgo-Marijuan, P.M. Martins, J.M. Queirós, R. Gonçalves, A. Gutiérrez-Pardo, et al., Porous composite bifunctional membranes for lithiumion battery separator and photocatalytic degradation applications: toward multifunctionality for circular economy, Adv. Energy Sustain. Res. 2 (2021) 2100046.
- [3] C.M. Costa, V.F. Cardoso, P. Martins, D.M. Correia, R. Gonçalves, P. Costa, et al., Smart and multifunctional materials based on electroactive poly(vinylidene fluoride): recent advances and opportunities in sensors, actuators, energy, environmental, and biomedical applications, Chem. Rev. 123 (2023) 11392–11487.
- [4] J.P. Serra, N. Pereira, D.M. Correia, C.R. Tubio, J.L. Vilas-Vilela, C.M. Costa, et al., Carrageenan-based hybrid materials with ionic liquids for sustainable and recyclable printable pressure sensors, ACS Sustain. Chem. Eng. 10 (2022) 8631–8640.
- [5] D.M. Correia, J.C. Barbosa, J.P. Serra, R.S. Pinto, L.C. Fernandes, C.R. Tubio, et al., Comparative assessment of ionic liquid-based soft actuators prepared by film casting versus direct ink writing, Adv. Eng. Mater. 23 (2021) 2100411.
- [6] S. Bahl, H. Nagar, I. Singh, S. Sehgal, Smart materials types, properties and applications: a review, Mater. Today. Proc. 28 (2020).
- [7] A. Bhatnagar, S. Wagh, B. Singh, R. Agrawal, F. Khan, Smart Materials-A Review 4, 2016, pp. 10–12.
- [8] A.D.B.L. Ferreira, P.R.O. Nóvoa, A.T. Marques, Multifunctional material systems: a state-of-the-art review, Compos. Struct. 151 (2016) 3–35.
- [9] F. Blomsma, M. Pieroni, M. Kravchenko, D.C. Pigosso, J. Hildenbrand, A. R. Kristinsdottir, et al., Developing a circular strategies framework for manufacturing companies to support circular economy-oriented innovation, J. Clean. Prod. 241 (2019) 118271.
- [10] S.M. Gonçalves, J.F.G. Motta, R. Ribeiro-Santos, D.W.H. Chávez, N.R. de Melo, Functional and antimicrobial properties of cellulose acetate films incorporated with sweet fennel essential oil and plasticizers, Curr. Res. Food Sci. 3 (2020) 1–8.
- [11] D.M. Correia, L.C. Fernandes, P. Martins, C. García Astrain, C. Costa, J. Reguera, et al., Ionic liquid–polymer composites: a new platform for multifunctional applications, Adv. Funct. Mater. 30 (2020).
- [12] D. Zamel, A.U. Khan, Bacterial immobilization on cellulose acetate based nanofibers for methylene blue removal from wastewater: mini-review, Inorg. Chem. Commun. 131 (2021) 108766.
- [13] A.W. Jatoi, I.S. Kim, Q.-Q. Ni, Cellulose acetate nanofibers embedded with AgNPs anchored TiO2 nanoparticles for long term excellent antibacterial applications, Carbohydr. Polym. 207 (2019) 640–649.
- [14] V. Vatanpour, M.E. Pasaoglu, H. Barzegar, O.O. Teber, R. Kaya, M. Bastug, et al., Cellulose acetate in fabrication of polymeric membranes: a review, Chemosphere 295 (2022) 133914.
- [15] Y. Liu, H. Huang, P. Huo, J. Gu, Exploration of zwitterionic cellulose acetate antifouling ultrafiltration membrane for bovine serum albumin (BSA) separation, Carbohydr, Polym. 165 (2017) 266–275.
- [16] S. Magalhães, C. Fernandes, J.F.S. Pedrosa, L. Alves, B. Medronho, P.J.T. Ferreira, et al., Eco-Friendly Methods for Extraction and Modification of Cellulose: An Overview 15, 2023, p. 3138.
- [17] E.N. Bifari, S. Bahadar Khan, K.A. Alamry, A.M. Asiri, K. Akhtar, Cellulose acetate based nanocomposites for biomedical applications: a review, Curr. Pharm. Des. 22 (2016) 3007–3019.
- [18] U.G. Spizzirri, G. Cirillo, F. Iemma, Polymers and food packaging: a short overview, in: Functional Polymers in Food Science, 2015, pp. 1–8.
- [19] A. Rehman, Z. Jahan, F. Sher, T. Noor, M.B.K. Niazi, M.A. Akram, et al., Cellulose acetate based sustainable nanostructured membranes for environmental remediation, Chemosphere 307 (2022) 135736.

- [20] S. Monisha, S. Selvasekarapandian, T. Mathavan, A. Milton Franklin Benial, S. Manoharan, S. Karthikeyan, Preparation and characterization of biopolymer electrolyte based on cellulose acetate for potential applications in energy storage devices, J. Mater. Sci. Mater. Electron. 27 (2016) 9314–9324.
- [21] P.C. Ray, H. Yu, P.P. Fu, Toxicity and environmental risks of nanomaterials: challenges and future needs, J. Environ. Sci. Health C Environ. Carcinog. Ecotoxicol. Rev. 27 (2009) 1–35.
- [22] L. Xuan, Z. Ju, M. Skonieczna, P.-K. Zhou, R. Huang, Nanoparticles-Induced Potential Toxicity on Human Health: Applications, Toxicity Mechanisms, and Evaluation Models 4, 2023, p. e327.
- [23] T. Jaswal, J. Gupta, A review on the toxicity of silver nanoparticles on human health, Mater. Today: Proc. 81 (2023) 859–863.
- [24] M. Markiewicz, J. Maszkowska, V. Nardello-Rataj, S. Stolte, Readily biodegradable and low-toxic biocompatible ionic liquids for cellulose processing, RSC Adv. 6 (2016) 87325–87331.
- [25] A.M. de Ferro, P.M. Reis, M.R.C. Soromenho, C.E.S. Bernardes, K. Shimizu, A. A. Freitas, et al., Designing the ammonium cation to achieve a higher hydrophilicity of bistriflimide-based ionic liquids, Phys. Chem. Chem. Phys. 20 (2018) 19307–19313.
- [26] J. M.S.S. Esperança, M. Tariq, A.B. Pereiro, J.M.M. Araújo, K.R. Seddon, L.P. N. Rebelo, Anomalous and not-so-common behavior in common ionic liquids and ionic liquid-containing systems, Front. Chem. 7 (2019) 450.
- [27] J.P. Serra, L.C. Fernandes, N. Pereira, A. Fidalgo-Marijuan, J.M. Porro, C.M. Costa, et al., Humidity sensors based on magnetic ionic liquids blended in poly(vinylidene fluoride-co-hexafluoropropylene), ACS Appl. Polym. Mater. 5 (2023) 109–119.
- [28] B.D.D. Cruz, D.M. Correia, R. Polícia, N. Pereira, P. Nunes, M. Fernandes, et al., Photoluminescent alginate-based composite inks for anti-counterfeiting security and soft actuator applications, Chem. Eng. J. 472 (2023) 144813.
- [29] C. Mendes-Felipe, M. Salado, L.C. Fernandes, D.M. Correia, L. Ruiz-Rubio, M. Tariq, et al., Photocurable temperature activated humidity hybrid sensing materials for multifunctional coatings, Polymer 221 (2021).
- [30] L.C. Fernandes, D.M. Correia, C. García-Astrain, N. Pereira, M. Tariq, J.M.S. S. Esperança, et al., Ionic-liquid-based printable materials for thermochromic and thermoresistive applications, ACS Appl. Mater. Interfaces 11 (2019) 20316–20324.
- [31] Z. Wang, X. Hou, N. Duan, Y. Ren, F. Yan, Shape- and color-switchable polyurethane thermochromic actuators based on metal-containing ionic liquids, ACS Appl. Mater. Interfaces 13 (2021) 28878–28888.
- [32] Y. Chen, J. Zhu, H. Ma, L. Chen, R. Li, P. Jin, VO2/nickel-bromine-ionic liquid composite film for thermochromic application, Sol. Energy Mater. Sol. Cells 196 (2019) 124–130.
- [33] H. Ragones, S. Menkin, Y. Kamir, A. Gladkikh, T. Mukra, G. Kosa, et al., Towards smart free form-factor 3D printable batteries, Sustain. Energy Fuel 2 (2018) 1542–1549.
- [34] C.M. Costa, R. Gonçalves, S. Lanceros-Méndez, Recent advances and future challenges in printed batteries, Energy Storage Mater. 28 (2020) 216–234.
- [35] D.M. Correia, L.C. Fernandes, N. Pereira, J.C. Barbosa, J.P. Serra, R.S. Pinto, et al., All printed soft actuators based on ionic liquid/polymer hybrid materials, Appl. Mater. Today 22 (2021).
- [36] H.Y. Tsai, H.J. Hsu, S.S. Yu, Shape reprogramming of 3D printed ionogels by solvent exchange with deep eutectic solvents, Polym. J. 55 (2023) 1211–1223.
- [37] S.S. Robinson, K.W. O'Brien, H. Zhao, B.N. Peele, C.M. Larson, B.C. Mac Murray, et al., Integrated soft sensors and elastomeric actuators for tactile machines with kinesthetic sense. Extreme Mech. Lett. 5 (2015) 47–53.
- [38] C. Zhong, T. Sasaki, A. Jimbo-Kobayashi, E. Fujiwara, A. Kobayashi, M. Tada, et al., Syntheses, structures, and properties of a series of metal ion-containing dialkylimidazolium ionic liquids, Bull. Chem. Soc. Jpn. 80 (2007) 2365–2374.
- [39] M. Meredith, C. McMillen, J. Goodman, T. Hanusa, Ambient temperature imidazolium-based ionic liquids with tetrachloronickelate(II) anions, Polyhedron 28 (2009) 2355–2358.
- [40] D.M. Correia, P. Martins, M. Tariq, J.M.S.S. Esperança, S. Lanceros-Méndez, Low-field giant magneto-ionic response in polymer-based nanocomposites, Nanoscale 10 (2018) 15747–15754.
- [41] V.I. Petrenko, L.C. Fernandes, O.I. Ivankov, C.R. Tubio, M. Tariq, J.M.S. S. Esperança, et al., Structural organization of ionic liquids embedded in fluorinated polymers, J. Mol. Liq. 360 (2022) 119385.
- [42] N.S. Kasálková, P. Slepička, Z. Kolská, V. Svorcik, Wettability and Other Surface Properties of Modified Polymers, 2015.
- [43] Y. Yuan, T.R. Lee, Contact angle and wetting properties, in: G. Bracco, B. Holst (Eds.), Surface Science Techniques, Springer Berlin Heidelberg, Berlin, Heidelberg, 2013, pp. 3–34.
- [44] T. Huhtamäki, X. Tian, J.T. Korhonen, R.H.A. Ras, Surface-wetting characterization using contact-angle measurements, Nat. Protoc. 13 (2018) 1521–1538.
- [45] V.S. Kulkarni, C. Shaw, Chapter 2 surfactants, lipids, and surface chemistry, in: V. S. Kulkarni, C. Shaw (Eds.), Essential Chemistry for Formulators of Semisolid and Liquid Dosages, Academic Press, Boston, 2016, pp. 5–19.
- [46] J.P. Serra, R.S. Pinto, J.C. Barbosa, D.M. Correia, R. Gonçalves, M.M. Silva, et al., Ionic liquid based fluoropolymer solid electrolytes for lithium-ion batteries, Sustain. Mater. Technol. 25 (2020) e00176.
- [47] B. Hermenegildo, R.M. Meira, A.G. Díez, D.M. Correia, S. Ribeiro, J.P. Serra, et al., Ionic liquid modified electroactive polymer-based microenvironments for tissue engineering, Polymer 246 (2022) 124731.
- [48] A. Zare, A. Hasaninejad, A. Salimi Beni, A.R. Moosavi-Zare, M. Merajoddin, E. Kamali, et al., Ionic liquid 1-butyl-3-methylimidazolium bromide ([Bmim]Br) as a green and neutral reaction media for the catalyst-free synthesis of 1-amidoalkyl-2-naphthols, Sci. Iran. 18 (2011) 433–438.

- [49] T. Sudiarti, D. Wahyuningrum, B. Bundjali, I. Made Arcana, Mechanical strength and ionic conductivity of polymer electrolyte membranes prepared from cellulose acetate-lithium perchlorate, IOP Conf. Ser. Mater. Sci. Eng. 223 (2017) 012052.
- [50] V. Rivas-Orta, R. Antonio-Cruz, J.L. Rivera-Armenta, A. Mendoza-Martínez, R. Ramírez-Mesa, Synthesis and Characterization of Organogel from Poly(Acrylic Acid) with Cellulose Acetate 10, 2010.
- [51] S. Gopi, A. Pius, R. Kargl, K.S. Kleinschek, S. Thomas, Fabrication of cellulose acetate/chitosan blend films as efficient adsorbent for anionic water pollutants, Polym. Bull. 76 (2019) 1557–1571.
- [52] A.W. Cindradewi, R. Bandi, C.-W. Park, J.-S. Park, E.-A. Lee, J.-K. Kim, et al., Preparation and characterization of cellulose acetate film reinforced with cellulose nanofibril, Polymers 13 (2021) 2990.
- [53] S.K. Mahadeva, J. Kim, Electromechanical behavior of room temperature ionic liquid dispersed cellulose, J. Phys. Chem. C 113 (2009) 12523–12529.
- [54] A. Rivera-Galletti, C.R. Gough, F. Kaleem, M. Burch, C. Ratcliffe, P. Lu, et al., Silk-cellulose acetate biocomposite materials regenerated from ionic liquid, Polymers 13 (2021) 2911.
- [55] J. Cao, X. Sun, C. Lu, Z. Zhou, X. Zhang, G. Yuan, Water-soluble cellulose acetate from waste cotton fabrics and the aqueous processing of all-cellulose composites, Carbohydr. Polym. 149 (2016) 60–67.
- [56] R. Fernández de Luis, M.K. Urtiaga, J.L. Mesa, K. Vidal, L. Lezama, T. Rojo, et al., Short-Range and Long-Range Magnetic Ordering, in Third Generation Brannerite Type Inorganic – Organic Vanadates: [{Mn(Bpy)}(VO3)2]≈(H2O)1.16 and [{Mn (Bpy)0.5}(VO3)2]≈(H2O)0.62, Chem. Mater. 22 (2010) 5543–5553.

- [57] R. Fernández de Luis, J. Orive, E.S. Larrea, M.K. Urtiaga, M.I. Arriortua, Reversible solid-state transformation in {Ni2(H2O)2(Bpa)2}(V6O17) proved by synchrotron radiation: color and magnetic properties change, Cryst. Growth Des. 14 (2014) 659, 670
- [58] M. Nan, F. Wang, S. Kim, H. Li, Z. Jin, D. Bang, et al., Ecofriendly high-performance ionic soft actuators based on graphene-mediated cellulose acetate, Sensors Actuators B Chem. 301 (2019) 127127.
- [59] A. Reizabal, R. Gonçalves, A. Fidalgo-Marijuan, C.M. Costa, L. Pérez, J.-L. Vilas, et al., Tailoring silk fibroin separator membranes pore size for improving performance of lithium ion batteries, J. Membr. Sci. 598 (2020) 117678.
- [60] D.M. Correia, E. Lizundia, R.M. Meira, M. Rincón-Iglesias, S. Lanceros-Méndez, Cellulose nanocrystal and water-soluble cellulose derivative based electromechanical bending actuators, Materials 13 (2020) 2294.
- [61] D.M. Correia, E. Lizundia, L.C. Fernandes, C.M. Costa, S. Lanceros-Méndez, Influence of cellulose nanocrystal surface functionalization on the bending response of cellulose nanocrystal/ionic liquid soft actuators, Phys. Chem. Chem. Phys. 23 (2021) 6710–6716.
- [62] V.J. Robertson, A.R. Ward, P. Jung, The effect of heat on tissue extensibility: a comparison of deep and superficial heating, Arch. Phys. Med. Rehabil. 86 (2005) 819-825
- [63] G. Lee, G.Y. Bae, J.H. Son, S. Lee, S.W. Kim, D. Kim, et al., User-interactive thermotherapeutic electronic skin based on stretchable thermochromic strain sensor, Adv. Sci. 7 (2020).